# Unveiling a facile approach for large-scale synthesis of N-doped graphene with tuned electrical properties

**Maxim K. Rabchinskii[1], Sergei A. Ryzhkov[1,2], Maksim V. Gudkov[3], Marina V. Baidakova[1,2*], Svyatoslav D. Saveliev[2], Sergei I. Pavlov[1], Vladimir V. Shnitov[1], Demid A. Kirilenko[1,2], Dina Yu. Stolyarova[4], Aleksey M. Lebedev[4], Ratibor G. Chumakov[4], Maria Brzhezinskaya[5], Kseniya A. Shiyanova[3],Sergey V. Pavlov[6,7], Vitaliy A. Kislenko[6,7], Sergey A. Kislenko[6,8], Anna Makarova[9], Valery P. Melnikov[3] and Pavel N. Brunkov[1,2]**

[1] Ioffe Institute, Saint Petersburg, Russia
[2] ITMO University, Saint Petersburg, Russia
[3] N.N. Semenov Federal Research Center for Chemical Physics, Russian Academy of Sciences, Moscow, Russia
[4] NRC "Kurchatov Institute", Moscow, Russia
[5] Helmholtz-Zentrum Berlin für Materialien und Energie, Berlin, Germany
[6] Joint Institute for High Temperatures of RAS, Moscow, Russian Federation
[7] Skolkovo Institute of Science and Technology, Skolkovo Innovation Center, Moscow, Russian Federation
[8] Moscow Institute of Physics and Technology, Dolgoprudny, Russian Federation
[9] Institute of Chemistry and Biochemistry, Freie Universitat Berlin, Berlin, Germany

*E-mail: baidakova@mail.ioffe.ru

Received xxxxxx
Accepted for publication xxxxxx
Published xxxxxx

## Abstract

In this paper, we for the first time demonstrate efficient nitrogen doping of graphene oxide (GO) with nitrogen concentration of up to almost 5 at.% and desired type of the nitrogen species via modified Hummers' method. Using X-ray photoelectron spectroscopy (XPS), X-ray absorption spectroscopy (XAS) and Fourier transform infrared spectroscopy (FTIR) techniques, we have found out graphitic nitrogen to be the dominant type of the implemented nitrogen species. At the same time, the subsequent GO thermal reduction to graphene appears to result in a transformation of the graphitic nitrogen into pyridines and pyrroles. The mechanisms of the observed GO nitrogen doping and conversion of the nitrogen species are proposed, providing an opportunity to control the type and concentration of the implemented nitrogen within the approach. A two-time increase of the graphenes' conductivity is observed due to the performed nitrogen doping. Further comprehensive electrical studies combined with the transmission electron microscopy (TEM) and density functional theory (DFT) modeling have allowed us to estimate the conductivity mechanism and the impact of the implemented nitrogen. As a net result, a simple method to synthesize GO and graphene layers doped with specific nitrogen species is developed, which leads to new perspective applications for graphene, i.e. supercapacitors, catalysis, and sensors.

 

Keywords: graphene, N-Doping, graphene oxide, Mott conductivity

## 1. Introduction

Besides the exceptional physical properties [1], one of the remarkable features intrinsic to graphene is its versatility for chemical modification through either the grafting by various functional groups or implementation of heteroatoms (e.g., N, B, S, or P) [2,3]. This aspect provides intriguing possibilities to tune physical and chemical properties of graphene in a desirable manner. Particularly, magnetic and electronic properties [4,5], band structure [6], catalytic activity [7], electrochemical properties [8] of graphene can be modified in a wide range by means of graphene functionalization. Furthermore, graphene adhesion and wetting characteristics, as well as chemical reactivity, can be tailored to perfectly fit the polymer matrixes for the purpose of manufacturing polymer-based composites [9]. Accordingly, chemical modification of graphene substantially improves the performance of graphene-based materials in practical applications and opens new ways of using this nanocarbon material.

Within the set of the developed approaches and techniques for graphene derivatization the nitrogen doping (N-doping) has been proposed as the most promising and widely studied one [10,11]. Owing to its atomic size and electronic configuration, nitrogen readily substitutes carbon atoms in the graphene lattice with the formation of a number of species, such as pyridines, pyrroles, graphitic-N (or quaternary-N), pyridine-N-oxide, etc. (see Supplementary data, Figure S1). The presence of these species provides substantial influence on the graphene electronic structure due to the high electron-withdrawing ability of nitrogen. Particularly, doping with nitrogen atoms allows graphene transformation into p- or n-type semiconductor respectively, accompanied by the opening of a band gap [12]. Several groups have recently reported studies on metal-free N-graphene with enhanced catalytic activity toward oxygen reduction reaction (ORR) [13]. Furthermore, the pyrrolic-N plays an important role in tuning the magnetization of graphene as demonstrated experimentally and theoretically [14], whereas pyridinic-N and graphitic-N can increase the graphene quantum capacitance [15].

Over the past few years, various methods have been developed for the graphene N-doping, including chemical vapor deposition (CVD) growth [16], plasma treatment and ion implantation [17,18], electrochemical modification [19] and graphene oxide (GO) hydrothermal modification reduction using nitrogen-containing agents, such as hydrazine, ammonia, urea, or thermal reduction in the nitrogen-containing media [20-22]. The latter one is regarded as the most facile one, due to its ease of operation, gram-scale quantity of the prepared material and versatility for the modulation of the N species type and content. Particularly, Seo et al. also reported that N-doped graphene could be prepared by using $NH_4OH$ and $N_2H_4$ mixed solution as a reducing agent, and the N content can reach about 8.9 at.%, with the predominance of the pyrroles and pyridines [20]. Sliwak et al. prepared nitrogen-doped reduced GO with nitrogen content, ranging from 10.9 to 13.4 at.%, which is among the highest reported ones [21]. At the same time, Schultz et al. [22] indicated that subsequent thermal annealing of the GO films grafted with ammonia and nitrile species (N concentration up to 6.4 at.%) allows to tune the type and relative content of the N species with their conversion into pyridines and graphitic nitrogen at different temperatures.

Apart from the GO reduction using a nitrogen-containing reducing agent, a more attractive concept to obtain N-doped graphene is to use as a precursor GO already doped by nitrogen during the synthesis. This approach substantially facilitates the production of N-doped graphene because it removes constraints on the applied reduction method since now there is no need in using nitrogen-containing agents or the corresponding environment. Hence, material processing becomes more versatile. Particularly, convenient photoreduction methods combined with lithography techniques [23] can be used, or GO derivatization via liquid chemistry can be carried out. Moreover, for several applications N-doped GO, not graphene, is needed – such as the formation of drug-delivery and bioimaging systems based on photoluminescent GO platelets [24]. Using the common procedures of GO N-doping during the reduction the aforementioned goals cannot be achieved. Last but not least, conventional strategies for graphene N-doping using GO lead to the formation of hydrophobic rGO layers with corresponding problems of its stacking due to $\pi$-$\pi$ interaction and formation of unstable suspensions, difficult in processing and using for the manufacturing of high-quality films [25]. A more convenient approach would be to perform N-doping of GO without its reduction and, thus, retention of its hydrophilic nature with the subsequent processing or deposition followed by conversion into N-doped graphene or any graphene derivatives.

Probably, GO nitrogen doping can be achieved during the conventional Hummers oxidation since the used combination of concentrated sulphuric acid and sodium nitrate is equal to the mixed sulphuric and nitric acid, known to provide nitration reaction. Considering nitrogen readily

 

incorporates into the graphene network at the vacancies and the position with oxygen groups [26,27], conversion of nitrates into implemented nitrogen can be suggested by tuning the GO synthesis conditions. However, no reports regarding the successful GO N-doping via Hummers oxidation has been published yet.

Hereby we for the first time demonstrate that the use of nitrate salts within the conventional Hummers method does lead to the implementation of up to 4.9 at.% of nitrogen into GO. The obtained nitrogen content is within the common value of nitrogen-doping, sufficient enough to provide substantial modification of graphene electronic and electrochemical properties. Moreover, the relative concentration of the implemented nitrogen in graphtitic form, the most desired for graphene-based electronic applications, is up to 74%, which is among the highest reported rates (Supplementary Table S1). At the same time, the simple thermal annealing of N-rGO at 375 °C in the air resulted in the formation of N-doped rGO with retention of the nitrogen content as in GO, but the conversion of almost all graphitic-N into pyrrolic-N and pyridinic-N proceeds in this case. Further electric studies revealed that the performed N-doping of rGO resulted in about doubling of the material conductivity with the Mott variable range hopping (VRH) mechanism of conductivity in the material. Finally, the mechanism of the GO doping was also investigated, describing the processes resulting in an implementation of nitrogen and giving a hint of the processes, underlying graphite oxidation into graphene oxide.

## 2. Materials and methods

### *2.1 Chemicals*

We used the following reagents: sulphuric acid ($H_2SO_4$), 93%; potassium permanganate ($KMnO_4$); hydrogen peroxide ($H_2O_2$), 30%; sodium nitrate ($NaNO_3$), 99+%; hydrochloric acid (HCl), 37% (Sigma-Aldrich, Germany). All the chemicals were of analytical purity grade commercially available. There was no need to additionally purify the reagents. Natural graphite (GO-350, China) was used as a starting material for the GO synthesis.

### *2.2 Graphene oxide synthesis and reduction*

GO was synthesized using modified Hummers' method [28] with (denoted hereinafter as N-GO) and without (denoted as p-GO) using $NaNO_3$. p-GO was obtained as follows. 1 g of graphite powder and 0.1 g of KMnO4 were mixed in 25 mL of cold $H_2SO_4$ (T = 4 °C) and stirred at cooling to 5-7 °C by an ice bath for 30 min to form a suspension with a bluish tint. Then 0.5 g of $KMnO_4$ was slowly added in the blend at magnetic stirred for 30 min to yield a grey-green mixture at 5-7 °C. This mixture was heated to 38-40 °C by a water bath and stirred for 30 min to remove the green tint. After that, the mixture was cooled again and the next 0.5 g of $KMnO_4$ was introduced into the reaction followed by stirring and heating as described in the previous step. These operations were repeated until the total amount of $KMnO_4$ became equal to 3 g. The product was diluted by slow addition of 50 mL of water (the temperature should not exceed 90 °C). 75 mL of microwave heated water was added to the mixture and allowed to stir for 15 min. Then further 5 mL of $H_2O_2$ was slowly added to the solution to produce a yellow-brown colour paste. The resultant product was subsequently washed with 2.5% HCl several times to achieve $H_2SO_4$ concentration lower than 0.001% and next centrifuged/decantated with demineralized water to 0.005% concentration of HCl. As a result, the aqueous dispersion of the product was cleaned of large particles by passing through a filter with a mesh size of 200 μm. N-GO was synthesized by the same procedure with the addition of 2 g of $NaNO_3$ prior to the introduction of graphite into the $H_2SO_4$ and slight stirring of the obtained mixture during 10 days.

Thermal reduction of the p-GO and N-GO films was carried out by heating the corresponding samples at 375 °C for 4 h in the air. The obtained samples are designated hereinafter as p-rGO and N-rGO, respectively.

### *2.3 Characterization of the obtained samples*

The UV-Vis absorption spectra of the GO and rGO samples were collected with a Shimadzu-2450 spectrophotometer. Fourier transform infrared (FTIR) spectroscopy was performed on the Infralum-08 FTIR spectrometer equipped with the attenuation of total reflectance attachment.

The X-ray photoelectron spectra (XPS) were measured using the NanoPES experimental station at the Kurchatov Synchrotron Radiation Source (National Research Center Kurchatov Institute, Moscow). The ESCA module (SPECS) equipped with XR-MF microfocus X-ray source (Al Kα, 1486.61 eV) and Phoibos150 analyzer was used. The spectra were calibrated with respect to the Au 4f7/2 line (84.0 eV). A surface charging revealed for low-conducting GO samples was taken into account by the aligning their XPS spectra with respect to the C 1s line position (284.7 eV) for a well-conductive rGO samples. The quantification and curve fitting of the obtained XPS spectra were performed by using standard CasaXPS software. The C 1s spectra were fitted by Shirley background and a set of one asymmetric Doniach-Sunjic function (DS) and five symmetric Gaussian−Lorentzian product functions (Gaussian by 70% and Lorentzian by 30%) (GL(30)), while the N 1s spectra were fitted by only the GL(30) functions.

N K-edge X-ray absorption spectra (XAS) were recorded at the Russian-German beamline of electron storage ring BESSY-II at Helmholtz-Zentrum Berlin (Germany) using the

ultrahigh vacuum experimental station [29]. The XAS measurements were performed in the total electron yield (TEY) mode realized by sweeping the incident photon energy and simultaneously recording the sample drain current. The thus-obtained TEY XAS spectra were then subjected to appropriate normalization and smoothing.

The samples for the FTIR and XPS studies were obtained by depositing 100 μl of the initial aqueous suspensions of p-GO and N-GO with a concentration of 0.05 wt.% onto the surface of silica wafers and subsequent drying at room temperature for 12 hours. Graphite samples for the XPS measurements were prepared by depositing graphite powder on the conductive carbon-based scotch-tape. Each presented X-ray photoelectron spectrum is obtained by averaging the spectra collected from 5 points on the 4 different samples to exclude the effect of the samples' non-uniformity and obtain reliable data.

Size distribution of GO and rGO flakes in aqueous solution was determined by laser diffraction measurements using Mastersizer 2000 equipment. Transmission electron microscopy (TEM) images were acquired with a Jeol JEM-2100F microscope (accelerating voltage 200 kV, point-to-point resolution 0.19 nm). Samples for TEM were prepared by deposition of aqueous GO and rGO suspensions $7*10^{-4}$ wt.% in concentration onto conventional lacey carbon films. Scanning electron microscopy (SEM) images were collected with a JEOL microscope JSM-7001F. Monolayer films for SEM imaging were prepared by the Langmuir–Blodgett method. Surface morphology and thickness of the rGO films were analyzed with a Veeco Dimension 3100 atomic force microscope (AFM) operating in the tapping mode by using RTESP probes.

### *2.4 Electrical studies*

The analysis of electronic properties of the p-rGO and N-rGO samples was performed on the base of two-electrode measurements. The p-rGO and N-rGO films were deposited onto the surface of quartz substrates with two comb Au electrodes 80 nm thick separated by 500 μm. The electrode comb consisted of 8 pairs of the electrode bars. Temperature-dependent sheet resistance measurements were performed by applying a sweep voltage in the range 0-3 V and measuring current via Keithley 6487 picoammeter/voltage source. Samples were hosted on the cold finger of Janis closed cycle refrigerator system (CCS-450) equipped with cryogenic temperature controller (LakeShore model 335). The cryostat chamber was evacuated to high vacuum via Pfeiffer Turbo Pumping System (HiCUBE 80 eco). Current-voltage measurements were performed at each temperature point for both bias directions after temperature equilibrium was reached. The negligible effect of the contact resistance and accurancy of the performed 2-electrode measurements were verified by a comparative measurements of the N-rGO sample at room temperature using both 4-probe and 2-electrode techniques, demonstrating sheet resistance values of 96.7 kΩ/sq and 96.8 kΩ/sq, respectively.

### *2.5 Theoretical modelling*

The plane-wave density functional theory (DFT) calculations were performed using the Vienna ab initio simulation package (VASP) [30]. The projector-augmented wave (PAW) method [31] with the Perdew, Burke and Ernzerhof (PBE) exchange-correlation functional [32] was used to calculate the electronic structure of the model systems, simulating p-rGO and N-rGO samples (see Supplementary data, Figures S2 and S3, respectively). The Brillouin zone was sampled with a 7x7x1 Monkhorst-Pack k-points mesh for ionic optimization and self-consistent calculations. The cutoff energy of 500 eV was adopted. The systems were based on the 11x11 graphene supercell, which has dimensions of 27.12 x 27.12 x 15 $Å^3$ with the angle 60° between the axes located in the graphene plane. The optimized C-C bond length for pristine graphene was 1.42 Å, which is in accordance with our previous cluster DFT calculations [33] and the experimental results [34]. The geometry of the studied structures was first optimized using the steepest descent algorithm with the Universal Force Field (UFF), as implemented in the Avogadro package, and then optimized using the damped molecular dynamics with the energy convergence criterion of $10^{-3}$ eV.

## 3. Results and Discussion

### *3.1 N-doping of graphene oxide*

Figure 1 demonstrates (a) survey, high-resolution (b) C 1s and (c) N 1s spectra of the initial graphite, p-GO and N-GO samples. The graphite survey spectrum indicates the absence of any contaminating impurities in the material, especially nitrogen species. This fact is also emphasized by the low-intensive high-resolution N 1s spectrum (Figure 1c). Only a low-intensity O 1s peak is observed, which corresponds to the oxygen in the interlayer water. This assertion is verified by the fact that there are no oxygen-related peaks in the graphite C 1s spectrum. The only asymmetric C=C peak centered at 284.7 eV, corresponding to the perfect $sp^2$-conjugated graphene lattice, can be discerned [35].

Analogously to graphite, p-GO survey spectra is presented only by C 1s and O 1s peaks, although the latter one becomes dominating due to successful graphite oxidation and its conversion into graphene oxide. Further analysis of the p-GO C 1s spectrum shows that six peaks can be distinguished, related to carbon atoms of the pure graphene network and the ones functionalized by various basal and edge oxygen located groups. Particularly, in addition to the C=C peak, features at 284 eV and 285.1 eV appears. The origin of the former one is indeterminate, being explained either by the

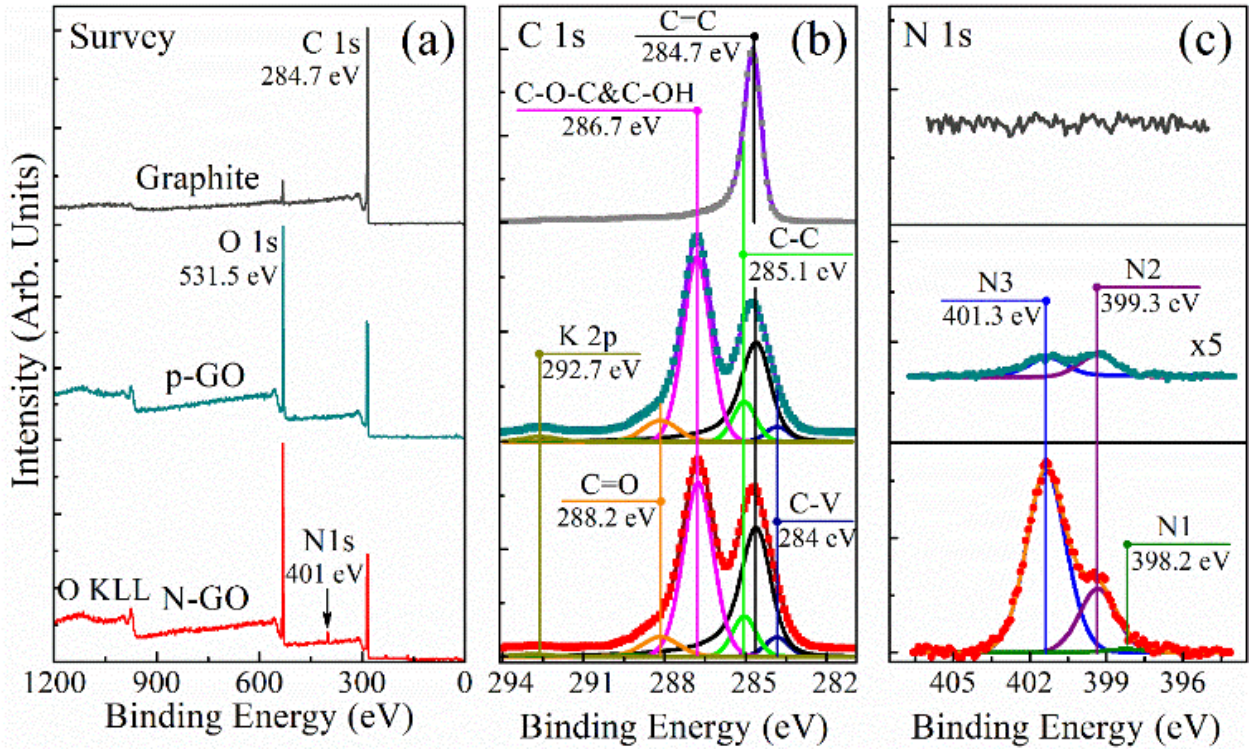


Figure 1. (a) Survey, (b) high-resolution C 1s and (c) high-resolution N 1s XPS spectra of the initial graphite, pristine graphene oxide (p-GO) and nitrogen-doped graphene oxide (N-GO).

presence of carbohydrate moieties (C-H/C-$H_2$) or carbon atoms of the graphene network located near or at the edges of vacancy defects [36]. The interpretation of the peak at 285.1 eV is more clear; it is assigned to carbon atoms, neighbouring the basal-plane oxygen groups which locally distort the graphene lattice [37]. Other three peaks positioned at 286.7 eV, 288.2 eV, and 292.7 eV are related to basal-plane hydroxyl and epoxide groups (C-OH&C-O-C), carbonyl groups (C=O) and potassium contaminates (K 2p), respectively [38, 39]. The C/O ratio calculated from the recorded C 1s XPS spectrum is estimated to be 1.82, pointing out the high degree of the GO oxidation with large content of the basal-plane hydroxyls and epoxides. At the same time, the N-GO sample exhibits slightly lower oxidation degree with C/O ratio of 1.95, what is still close to the highly-oxidized graphene oxide [40].

Despite the absence of the nitrogen signal in the survey spectrum, the p-GO high-resolution N 1s spectrum (Figure 1c) indicates the presence of nitrogen in a trace amount in the obtained material with the estimated content of less than 0.3 at.%. In comparison to the p-GO, the N-GO sample synthesized with the use of sodium nitrate contains a significant amount of nitrogen what is signified by the distinguishable N 1s peak in the survey spectrum. The performed calculations show that concentration of the nitrogen is about 4.9 at.%. This value is almost equal to the nitrogen content commonly reached after GO and rGO nitrogen doping via various methods, for instance by chemical treatment with ammonia, hydrazine, melamine, etc. [20-22, 41], as well as by nitrogen implantation using $N^+$ ion bombardment without amorphization of the graphene layer [17, 18].

To analyse whether the detected nitrogen is related to the molecular moieties, contaminating the studied samples, or is incorporated into the structure of the graphene oxide the obtained p-GO and N-GO N 1s spectra were deconvoluted. Three peaks positioned at 398.2 eV, 399.3 eV, and 401.3 eV were distinguished, corresponding to pyridinic-N (N1), pyrrolic-N (N2), and graphitic-N (N3), respectively. These assignments are quite common [20, 22, 42]. In the p-GO pyrroles and graphitic nitrogen are almost in equal relative concentrations (52% and 48%, respectively). On the other hand, in the N-GO sample graphitic nitrogen is a dominant specie, presenting about 74% of all the incorporated nitrogen, whereas the relative content of the pyridines and pyrroles is determined to be 1.37% and 24.52%, respectively.

The obtained results evidence that the nitrogen doping does proceed during the synthesis of GO using the Hummers oxidation method, since no nitrogen is detected in the initial graphite. Interestingly, the same effect can be found out in the series of published articles devoted to GO synthesis [33, 43-45], where the N 1s signal is observed in the displayed XPS survey spectra, although it was not emphasized by the authors. Obviously, in the case of the N-GO, the nitrogen

source is sodium nitrate, but it is excluded from the p-GO synthesis protocol and the formation of even small amounts of the nitrogen species in this material on the first sight is somewhat unexpected. However, the further precise analysis of the reagents used during the synthesis revealed that the used sulphuric acid contains a small amount of nitric acid due to the $H_2SO_4$ production technology. This is the origin of a modest nitrogen doping of the p-GO, which, thus, proceeds by the same mechanism as in the case of N-GO.

Given these results, the mechanism for the GO N-doping during the synthesis was proposed. The mix of concentrated $H_2SO_4$ and $HNO_3$ is known to provide nitration of the organic compounds, such as benzene, anthracene, etc., due to formation of reactive N $O_2^+$ species:

$$2H_2SO_4 + HNO_3 \rightarrow 2HSO_4^- + NO_2^+ + H_3O^+ \quad (1)$$

In the case of sodium nitrate ($NaNO_3$) or other alkali metal nitrates instead of nitrate acid the same reaction proceeds, but with an additional step:

$$2NaNO_3 + H_2SO_4 \rightarrow 2HNO_3 + H_2SO_4 \quad (2)$$

Thus, nitration of the graphene layers at the edges and local defects, particularly vacancies, can proceed during the GO synthesis via Hummers method along with bonding of sulphate esters (Figure 2b). This suggestion of the covalent attachment of the $–NO_2$ during the N-GO synthesis was verified by the high-resolution N 1s XPS and FTIR spectra of the N-GO sample (Figure 3), withdrawn from the reaction mixture prior to the hydrolysis procedure (GO-Nit). As seen, along with the N1-N3 nitrogen peaks spectral feature at ~406.5 eV additionally appears, which corresponds to $–NO_2$ moieties [46]. Moreover, this peak is the dominant one, suggesting the highest relative concentration of the nitrates in comparison to graphitic-N, pyrrolic-N and pyridinic-N. Nitrogen content calculated by the comparison of the relative areas of N 1s and C 1s (see Supplementary data, Figure S4) peaks is estimated to be ~4 at.%. The presence of the nitrates as well as nitrate esters is also indicated by the distinguishable bands at 1280 $cm^{-1}$, 872 $cm^{-1}$ and 1160 $cm^{-1}$ in the FTIR spectrum. These absorption bands disappear after the completion of the N-GO synthesis and elimination of the nitrate groups indicated by the N-GO N 1s spectrum.

Nitrate group is chemically stable. However, in the acid medium it can transform into aci form – nitronic acid (also called azinic acid, -$NOOH_2$) [47] – which is much more chemically reactive (Figure 2c). In most cases, the formed nitronic acid transforms back to nitrate due to its intrinsic instability. However, with some probability, in acidic medium the formation of nitronic acid can be followed by the dehydration reaction with formation of the water molecule and subsequent bonding of the nitrogen atom to the edge located carbon atoms of graphene network, forming pyridine N-oxide moiety (Figure 2d). Formed at the edge of the vacancy in graphene network, pyridine N-oxide further can react with the carbon atom at the edge of graphene network with formation of ester (Figure 2e). In the presence of the

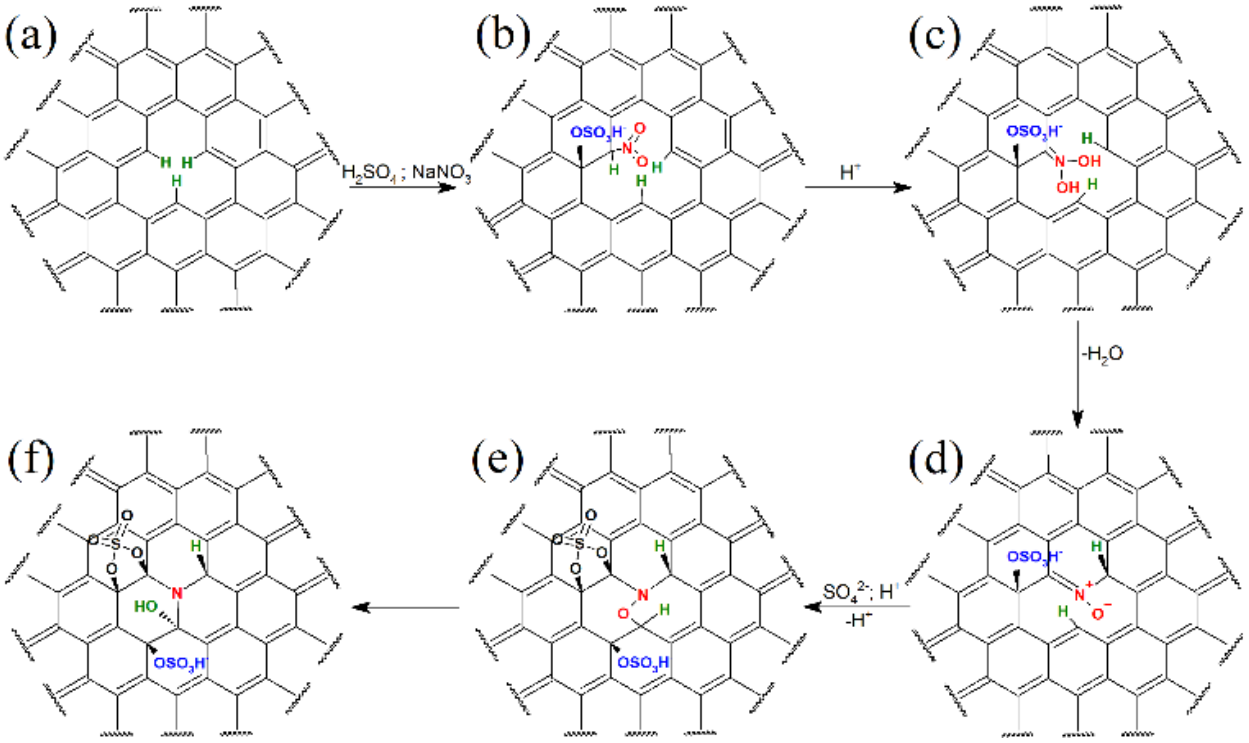


Figure 2. Scheme of the GO N-doping during the synthesis due to the presence of nitrates at the defect sites of graphene network.

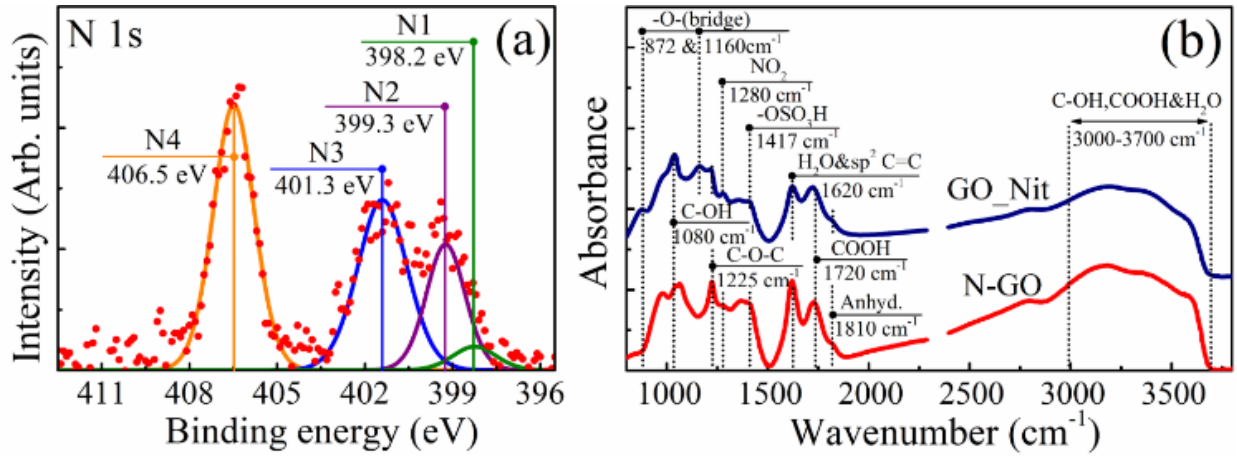


Figure 3. (a) High-resolution N 1s XPS spectrum and (b) FTIR spectra of the GO-Nit. N-GO FTIR spectrum is shown for the comparison

hydrogen atoms from carbohydrate groups $CH/CH_2$, this intermediate structure further transforms, resulting in the formation of hydroxyl group [48] and implementation of the nitrogen into the graphene network, forming graphitic-N (Figure 2f). Apparently, in the case of sub-nanometer holes where nitrogen atom can be coordinated only by two carbon atoms, pyridinic-N and pyrrolic-N are formed as a result of the described process.

Tendency of the nitrogen incorporation in various forms at the areas of vacancies and the position with oxygen-containing functional groups was already demonstrated, both theoretically and experimentally [24, 25]. Obviously, the concentration of the implemented nitrogen by the proposed reaction depends on the concentration of vacancy defects, both initially presented and formed during the oxidation [49], and the duration of the intercalation process, which determines the number of the nitrate groups transitions into aci form. These factors explain the variation of N content after the GO synthesis which can be indicated in various works [42, 43, 50]. In our case, the intercalation of graphite by the mix of concentrated $H_2SO_4$ and $NaNO_3$ is carried out during 10 days, in order to completely exfoliate the graphite. This sufficiently longer in comparison to the conventional approaches for the GO synthesis, resulting in an effective GO N-doping.

### *3.2 Thermally driven conversion of the N-GO into nitrogen-doped graphene layers*

To further assess the possibility to obtain N-doped graphene layers from the synthesized N-GO and analyse the evolution of the type and concentration of the nitrogen species in the obtained material, N-GO films were reduced via thermal annealing at 375 °C in the air. Figure 4 shows the high-resolution C 1s and N 1s XPS spectra of the reduced N-

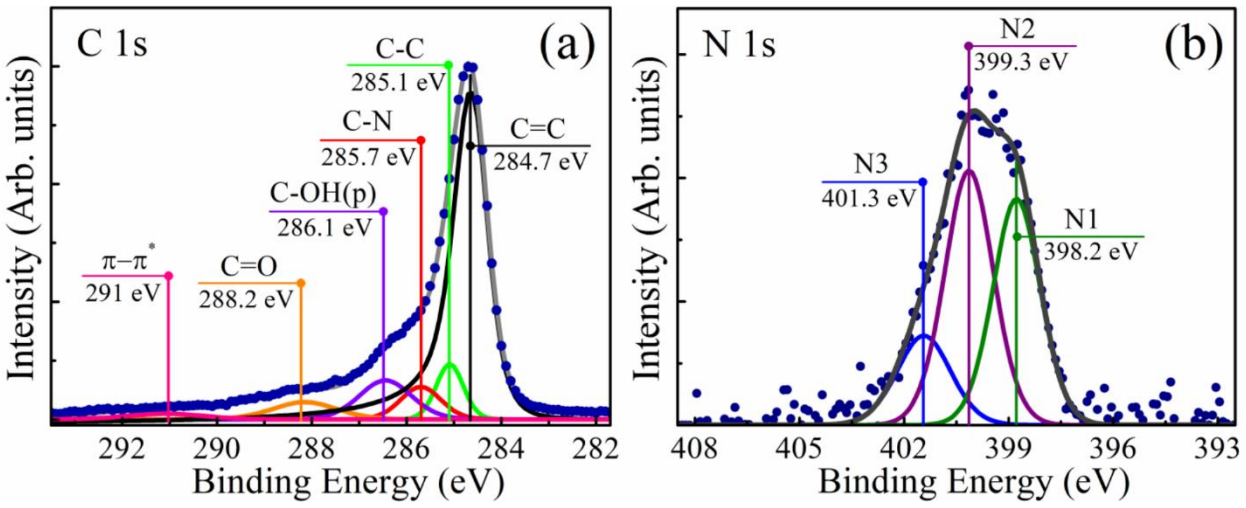


Figure 4. High-resolution (a) C 1s and (b) N 1s XPS spectra of the nitrogen-doped graphene oxide after its thermal reduction (N-rGO).

GO (N-rGO). Upon the reduction most part of the oxygen moieties, particularly basal-plane hydroxyls and epoxides, had been removed as is evidenced by the complete elimination of the C-OH&C-O-C peak and a significant decrease in the intensity of the C=O peak. The restoration of the $sp^2$-conjugated graphene network is also indicated by the appearance of the $\pi$-$\pi^*$ shakeup satellite of the peak C=C at 291 eV and the changes in the UV-Vis absorption spectra (see Supplementary data, Figure S5). On the other hand, a new peak at 286.1 eV appears (C-OH(p), corresponding to the edge-located phenols, known to form upon the thermal reduction and be highly stable at temperatures below 800 °C [51, 52]. Additionally, C-N peak at 285.7 eV is now resolved in the measured C 1s XPS spectrum, being earlier masked by the dominating C-OH&C-O-C peak. The N-GO reduction results in the rise of C/O ratio to 12.1, what is of the same order to those values obtained for rGOs commonly prepared via thermal annealing and chemical reduction. Besides the removal of the oxygen moieties, the concentration of the nitrogen remained almost the same after the reduction as is seen from the comparison of the N-GO and N-rGO survey spectra (see Supplementary data, Figure S6). The subsequent quantitative analysis of the latter one gives the value of nitrogen content around 4.83 at.%. On the other hand, significant changes in the composition of the nitrogen species occur upon the transition from N-GO to the N-rGO (Figure 4b). The relative concentration of the graphitic nitrogen reduced by almost 4 times, from the 74% to 19.1%. Oppositely, the pyridine and pyrrole groups became the dominant ones, with the relative concentrations of 37.4% and 43.5%, respectively. The conversion of the graphitic nitrogen into the pyrrolic and pyridinic forms is also demonstrated by the obtained N K-edge XAS spectra (Figure 5). The well-resolved features commonly observed in the near edge X-ray absorption spectra provide a more reliable means of distinguishing between the different nitrogen local bonding environments as compared to the overlapping peaks observed in XPS spectra [22]. In the spectrum of the N-GO two distinct resonances at 400.9 eV (N3) and 405.4 eV (N5) are resolved.

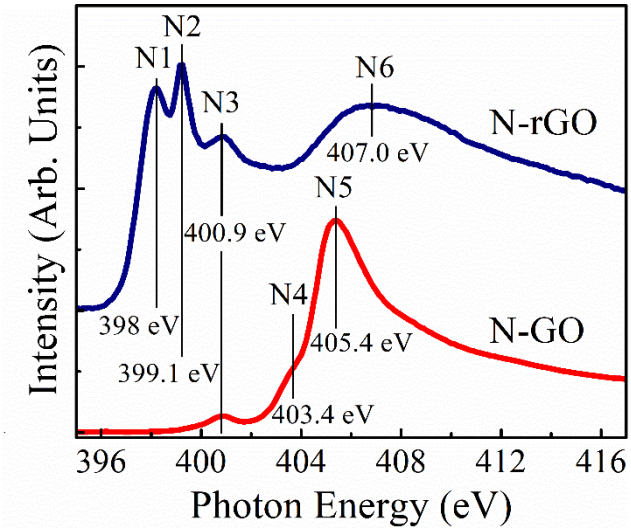


Figure 5. N K-edge XAS spectra of the N-GO and N-rGO samples.

The former one corresponds to electronic transitions to $\pi^*$ states associated with the graphitic nitrogen. The narrow intensive resonance centered at 405.4 eV is ascribed to transitions from N 1s core levels to unoccupied C–N $\sigma^*$ and C=N $\sigma^*$ orbitals. These assignments of the spectral features are generally concordant with literature reports of the N K-edge spectral signatures of sy stems ranging from molecules to amorphous carbon nitride thin films and CVD-grown N-doped graphene [11, 21, 53]. Additionally, a shoulder centered around 403.4 (N4) can be discerned, most probably attributed to transitions to $\pi^*$ states localized on pyridine-N-oxide or nitrate moieties, considering its energy. After the thermal treatment, new well-resolved narrow (C=N) $\pi^*$ resonances at 398 eV (N1) and 399.1 eV (N2) arise and become the dominant ones, although the N3 feature also remains in the N-rGO XAS spectrum. The resonances N1 and N2 are attributed to the transitions from N 1s states to $\pi^*$ levels associated with pyridinic and pyrrolic nitrogen, respectively [10, 53]. Note that the relative energy positioning (N1 < N2 < N3<N4) corroborates the suggested XPS assignments, noted above. Along with the appearance of the new $\pi^*$ resonances, the $\sigma^*$ resonance significantly broadens and shifts to the higher energies (N6). This is a result of the increase in the number of various configurations of the C-N bonds, which induces the broadening of the nitrogen-associated $\sigma^*$ resonance.

Earlier Schultz et al. has demonstrated that thermal annealing of the GO grafted with the nitrile and amine groups leads to the progressive transformation of these species into in-plane pyridinic and then into graphitic moieties [22]. Importantly, it was demonstrated that the graphitic nitrogen to be the most stable form of the incorporated nitrogen after the annealing at 1000 °C, whereas pyridinic nitrogen was shown to be the dominant nitrogen specie after the GO thermal reduction at the range of temperatures from 300 to 750 °C. Our results coincide with this data, although here we observe the transformation of the initially present graphitic nitrogen into pyrroles and pyridines. This can be explained in the terms of the defect formation in the graphene layer, particularly vacancies and subnanometer-size holes, during the GO thermal annealing at the temperatures below 800 °C, what is widely discussed in the literature [54, 55]. Owing to the formation of these defects as a result of oxygen functionalities elimination, the initially presented graphitic nitrogen can become located at the boundary of the graphene lattice with the elimination of one of the neighbouring carbon atoms and can be converted

into the pyridine or pyrrole moiety (see Supplementary data, Figure S7). The formation of the latter one additionally requires the source of hydrogen, which is presented by the reaction of the hydroxyls and carboxyls elimination, in which CO and $CO_2$ molecules are formed [55, 56] and hydrogen is bonded to graphene network as C-H group or, in our case, as an N-H part of pyrrole.

### *3.3 Electrical properties and electronic structure of the N-doped graphene films*

To analyse how the performed rGO nitrogen doping modifies the electronic properties of the obtained material set of the comparative studies of the N-rGO and pristine rGO (p-rGO) films was carried out. p-rGO was prepared via the same thermal annealing procedure from the nitrogen-free p-GO and exhibits a comparable degree of the reduction as is shown by the obtained C 1s XPS spectra (see Supplementary data, Figure S8). The p-rGO C/O ratio is calculated to be 11.4. Moreover, flakes of both N-rGO and p-rGO exhibit equal structural quality and the mean lateral size as is determined by the means of TEM imaging and analysis of the SEM images and results of LD measurements (see Supplementary data, Figures S9 and S10). Hence, the potential difference between electrical properties of the N-rGO and p-rGO films with identical thickness would originate from the incorporation of N species into the graphene network.

Figure 6a shows the voltage (V) versus current (I) characteristics plot of N-rGO and p-rGO obtained within the range of -3 to 3 V. The linear behavior confirms the good Ohmic contact between the films and electrodes. The sheet resistance and electrical conductivity were calculated considering the geometry of the films and averaged over several measurements. The sheet resistance values at room temperature are found to be 54 kΩ /sq and 98 kΩ /sq, for the N-rGO and p-rGO samples, respectively, giving conductivity values of 2300 and 1270 S/m. The collected electrical data clearly shows that the provided nitrogen doping almost doubles the conductivity of the rGO layer. This can be attributed to the participation of the graphitic-N lone pair in the electron delocalization in the graphene network, enhancing the π electrons conjugation of graphene network and leading to the rise of the graphene layer conductivity. Earlier this effect was demonstrated by Park et al. [57] for the rGO nitrogen doping via hydrazine with formation of pyrazoles, six-membered aromatic rings, which contain two nitrogen atoms and similar by its electronic structure to graphitic-N. At the same time, pyridinic-N and pyrrolic-N cannot participate in the discussed process as the lone pair electrons of nitrogen in this species does not involve in the formation of delocalized π-conjugated system. Thus, the observed conductivity enhancement can be further improved by the applying other method for N-GO reduction, for instance, photochemical reduction of hydrazine treatment, which will not result in conversion of graphitic-N into pyrrolic and pyridinic ones. In this case, the total concentration of graphitic-N could be raised from the observed 0.93 at.%, considering the aforementioned relative content obtained from N 1s XPS spectrum, to about 3-4 at.% with the corresponding rise of the conductivity.

It is worth noting that the common drawback of the nitrogen incorporation into graphene layer, is formation of the additional scattering centers for the electron transport, such as nitrogen induced defects and graphitic-N by itself,

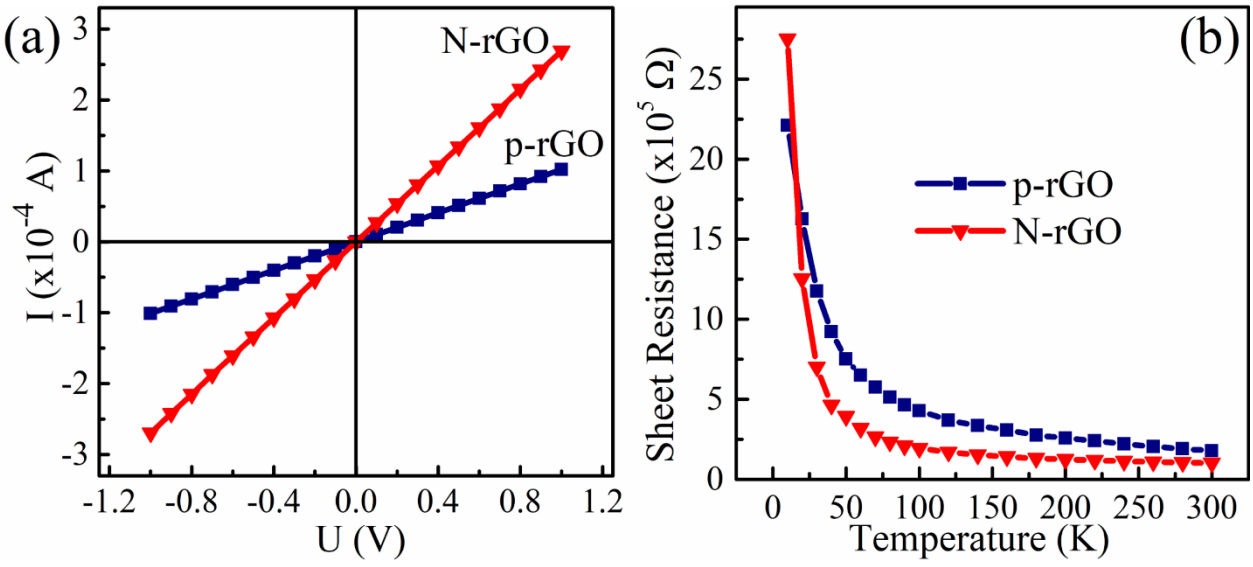


Figure 6. (a) I-V curves (T=300 K) and (b) semi-log scale plot of resistance versus temperature for N-rGO and p-rGO films, 15 nm thick.

thus leading to the commonly observed lowering of the N-doped graphene conductivity [12, 57]. However, if the N species are localized in clusters [11] and various range hopping mechanism dominates instead of ballistic transport, the effect of charge scattering on the nitrogen species would diminish. Temperature dependence of the sheet resistance in the temperature range from 10 to 300 K was further measured, giving a hint of the mechanisms of N-rGO and p-rGO electrical conductivity. The ohmic behavior for both samples within the whole range of temperatures, except 10 K, in the voltage range from 0 to 3 V (see Supplementary data, Figure S11) was observed. In the case of 10 K slight non-linearity of the I-V curve was detected. The values of R for each sample were further measured at a fixed low bias voltage of 1 V with a delay of 100 ms after reaching the selected temperature. Figure 6b shows a semi-log scale plot of R versus (vs) T. As seen, over a broad temperature range the sheet resistance decreases rapidly for more than 2 orders of magnitude with temperature. This is a distinctive feature of the semiconducting nature of the films, evidencing the VRH mechanism of conduction in the obtained materials, which is characterized as:

$$R(T) = R_0 \exp\left(\frac{T_0}{T}\right)^p \quad (3)$$

where $R_0$ is a pre-factor, $T_0$ is a characteristic temperature and p is a characteristic exponent the value of which distinguishes different types of VRH mechanism [58 – 61]. Particularly, Mott variable range hopping (Mott-) and Efros-Shklovskii (ES-) VRH conduction mechanisms are commonly distinguished while studying the rGO and modified graphenes. The Mott-VRH considers a constant density of states (DOS) near the Fermi level ($E_F$) and corresponds to the low disorder and functionalization level of the material, giving a value of p equal to 1/3 for the 2D systems [59, 60]. On the other hand, the ES-VRH regards the fact that DOS near the $E_F$ is not constant rather it vanishes linearly with energy for a 2D system [61, 62], what is commonly observed at low temperatures and also due to low structural quality and a high number of functionalities. In the case of ES-VRH p=1/2.

The usual practice of determining the type 2D hopping conduction mechanism is by plotting ln R vs either $T^{-1/3}$ (Mott-VRH) or $T^{-1/2}$ (ES-VRH). As seen from Figure 7a, the temperature dependence of ln R for both N-rGO and p-rGO samples almost perfectly fit the $T^{-1/3}$ behaviour within the 30-300 K temperature range. At the same time, the obtained data cannot be fitted very well in the $T^{-1/2}$ –scale (see Supplementary data, Figure S12). It can be also seen that there is a deviation from the Mott-VRH model below ~20 K, however the obtained data is not sufficient enough to determine whether it is related to transition from Mott-VRH to ES-VRH mechanism or is an experimental feature.

In order to analyse the type of the VRH mechanism more precisely, the dimensionless energy of activation W, which can be obtained from the Eq.1 as a logarithmic derivative [63]:

$$W = \frac{\partial ln R(T)}{\partial ln T} = p \times \left(\frac{T_0}{T}\right)^p \quad (4)$$

was analysed. Figures 7b and 7c show lnW vs lnT plot for the N-rGO and p-rGO samples, respectively. The presented curves clearly demonstrate that the data follow the p = 1/3 line for both materials. From the slopes of the plots the accurate values of p were obtained, estimated to be p=0.3104 for the N-rGO and p=0.3367 for the p-rGO. Additionally, the extrapolation of the resistance to temperature dependence curves to the $T^{-1/3}=0$ in the Figure 7a allowed us to obtain the

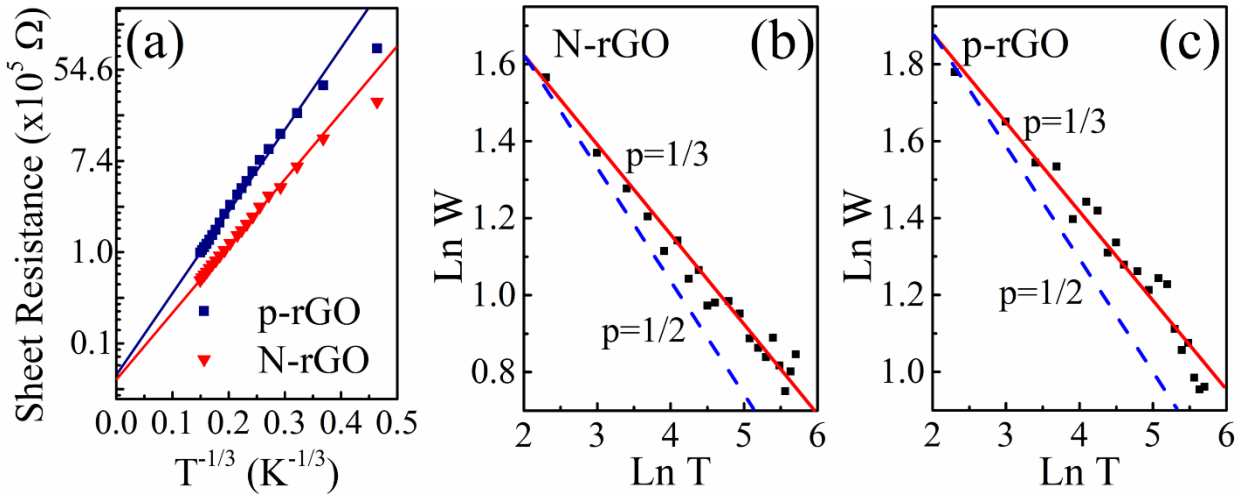


Figure 7. (a) The resistivity ln R versus T-1/3 for N-rGO and p-rGO samples. The symbols are the experimental points and the solid lines are a fit to T−1/3 behaviour. (b, c) Reduced activation energy (W) plotted vs temperature (T) in a log-log scale for N-rGO and p-rGO samples. For a better comparison lines with p = 1/2 (ES-VRH) and p = 1/3 (2D Mott-VRH) are.

value of pre-factor $R_0$. One can see, that both traces merges at an almost same $R_0$, giving values of 6.997 kΩ and 6.225 kΩ for p-rGO and N-rGO, respectively. Collectively, the fine fit of the lnR curves with $T^{-1/3}$, the values of p=1/3 obtained from the lnW vs lnT plot and the universal value of R0 for both N-rGO and p-rGO unambiguously indicates that these materials exhibit the same type of the VRH conductivity mechanism, which is determined to be Mott-VRH mechanism. This result is in consistent with the previous reports of Mott-VRH in variously obtained rGO layers [64, 65], asserting absence of any considerable effect of the performed N-doping on the conductivity mechanism in the rGOs at the 20-300 K range of temperatures. However, still more precise analysis of the resistance vs temperature dependence within the temperature range of 1-10 K is needed to clarify the features of the obtained materials conductivity parameters.

Given the lnR vs $T^{-1/3}$ plot and the obtained $R_0$, the characteristic temperature $T_0$ values can be further evaluated using eq.3. Hence, the changes of the localization length, thus the delocalization degree, can be analysed, using the following equation:

$$T_0 = \frac{3}{k_B N(E_F)\xi^2} \quad (5)$$

where ξ is the localization length and $N(E_F)$ is the DOS around the Fermi level. The values of T0 are determined to be 5936 K and 2790 K for the p-rGO and N-rGO films, respectively. However, it is challenging to determine the $N(E_F)$ values experimentally. Therefore, we performed the theoretical calculations to obtain DOS spectra for the p-rGO and N-rGO layers and, thus, estimate the difference in the $N(E_F)$ values due to the N-doping. The calculated p-rGO and N-rGO structures are presented in Supplementary data, Figure S2 and S3, respectively. For representativeness, four pairs of systems were considered, differing in the size and number of holes. The structures consider formation of the vacancies and defects due to the thermal annealing. The total and relative concentration of the nitrogen species in the N-rGO system was chosen to fit the experimental results. To obtain DOS spectra, data on the electronic structure of corresponding systems were averaged. The DOS spectrum of the pristine graphene is additionally presented as a reference.

As seen from the obtained DOS spectra (Figure 8a) formation of vacancies and sub-nanometer holes increases the number of states within the region of 0 – 1.5 eV below the

Fermi level with the appearance of the local maximum centered at ca. -1.1 eV. The increase of DOS in the near-Fermi region due to the perforation of the graphene lattice was earlier demonstrated [66, 67]. In the case of the N-rGO, one can see a slight shift of the DOS minimum to the left from the Fermi level due to the n-doping effect of the nitrogen groups. It is worth noting that only graphitic-N has

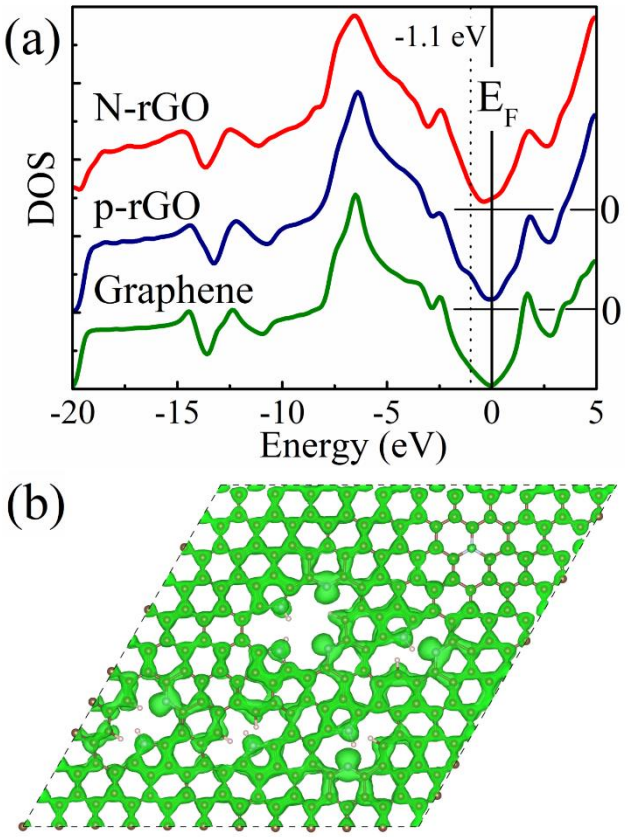


Figure 8. (a) Theoretically calculated DOS spectra of the pristine graphene, p-rGO and N-rGO. The spectra are aligned respectively to the $E_F$ of the pristine graphene. (b) charge density plot of the electronic states at the energies [-3; -1] eV.

the effect of n-type doping, an increase in the concentration of which could lead to a larger shift of the Fermi level. This coincides with the published results, demonstrating that graphitic-N results in the graphene n-doping [10, 68]. Also the increase of the $N(E_F)$ in the range of [-3; -1] eV with the sharp peak at ca. -2 eV is observed in the case of N-rGO system, arising due to the states related to doping N species as is indicated by the calculated partial DOS associated with nitrogen (see Supplementary data, Figure S13). One can see that significant part of the electron density in the [-3; -1] eV energy range localized on the nitrogen groups pyridinic and pyrollic nitrogen groups (Figure 8b), due to the localized lone pair electronic states, which are main active sites for the oxygen reduction reactions (ORR) and sorption of hydrogen atoms [69 – 71].

Based on the calculated DOS spectra, the average value of the density of states in the corresponding energy ranges [-ΔE;ΔE] near the Fermi energy can be estimated. To consider the relevant ΔE value we have estimated the hopping energy using the following equation [72]:

$$\Delta E = kT\left(\frac{T_0}{T}\right)^{1/3} \quad (6)$$

Using this relation, the ΔE values for p-rGO and N-rGO for the temperature of 300K were calculated to be 0.07 eV and 0.05 eV. In this case, the average value of the density of states in the corresponding energy ranges [-ΔE; ΔE] relative to the Fermi energy are $8.5*10^{-3}$ $eV^{-1}$ $A^{-2}$ for p-rGO and $2*10^{-2}$ $eV^{-1}$ $A^{-2}$ for N-rGO. Consequently, according to the eq.5 the localization lengths are 2.63 nm and 2.44 nm, respectively. This is in good coincidence with the results of determining lateral size of the $sp^2$-domains in the reduced graphene oxide by means of high-resolution TEM or Raman spectroscopy [73, 74]. At the same time, the almost equal values of the localization length indicate that the presence of implemented nitrogen species does not significantly increase the graphene layer disordering at these concentrations of the doping.

## 4. Conclusions

In conclusion the results presented here show that the GO synthesis via conventional Hummers oxidation with the use of sodium nitrate results in N-doping of the obtained graphene oxide, reaching almost 5 at.% of the introduced nitrogen species. This effect was not discussed earlier, although some evidence of the GO N-doping after the synthesis can be found in various published articles. Considering the proposed mechanism, the concentration of the incorporated nitrogen can be tuned by the variation of the duration of graphite exfoliation in the mix of concentrated sulfuric acid and sodium nitrate as well as by changing the latter one to sodium nitrite.

The implemented nitrogen is predominantly presented in the form of graphitic-N, highly desirable for the modulation of graphene and rGO electronic properties. However, the thermal reduction leads to conversion of graphitic-N into the pyridinic-N and pyrrolic-N. This effect can be neglected by applying another reduction technique, particularly photochemical treatment or chemical reduction, what will be discussed in the forthcoming paper.

Moreover, the retention of about 1 at.% of the graphitic-N with about 4 at.% of pyridinic-N and pyrrolic-N still results in almost doubling the rGO layer conductivity due to the provided n-doping and corresponding increase of the DOS near the Fermi level. At the same time, the conductivity mechanism in both N-doped and pristine rGO is determined to be the same, corresponding to the Mott-VRH mechanism, with almost the equal localization length. Hence, the key impact of the implemented nitrogen species on the graphene electronic structure is due to the modification of the DOS spectra near to the Fermi level.

As a net result, a facile method to obtain N-doped GO and graphene layers with the desired type of the nitrogen species is proposed as well as new details on the GO synthesis using the Hummers approach are revealed.

## Acknowledgements

M. K. Rabchinskii, M.V. Baidakova, V.V. Shnitov and D.A. Kirilenko work on XPS, XAS and electrical studies in subsections 3.1, 3.2 and 3.3 was supported by the grant of the Russian Science Foundation (Project No. 19-72-10052). S.I. Pavlov and S.A. Ryzhkov acknowledge the Russian Foundation for Basic Research (grant no. 18-29-19172) for the support of the experiments on the chemical synthesis in the subsection 3.1. M.V. Gudkov thanks the Program of Fundamental Researches of the Russian Academy of Sciences (project № 0082-2019-0008) for financial supporting. V.P. Melnikov thanks the Program of Fundamental Researches of the Russian Academy of Sciences (project № 0082-2019-0004) for financial supporting. S.V. Pavlov's, S.A. Kislenko's and V.A. Kislenko's work on DFT modelling in subsection 3.3 was supported by the state assignment of JIHT RAS (Theme No. AAAA-A19-119022190058-2). D Yu. Stolyarova thanks for support NRC "Kurchatov Institute".

The experiments were carried out on the equipment of the Joint Research Center "Materials science and characterization in advanced technology" with financial support by Ministry of Education and Science of the Russian Federation (id RFMEFI62119X0021) and the Unique Scientific Equipment "Kurchatov Synchrotron Radiation Source".

M. K. Rabchinskii, V. V. Shnitov, M. V. Baidakova, D. Yu. Stolyarova and M.V. Gudkov thank Helmholtz-Zentrum Berlin (HZB) for the allocation of synchrotron radiation beamtime and Russian-German Laboratory at HZB (Germany) for the financial support of their XPS and XAS measurements.

The computations were carried out using supercomputers at Joint Supercomputer Center of the Russian Academy of Sciences (JSCC RAS) and Skoltech CDISE supercomputer "Zhores" [75].

There are no conflicts of interest to declare.

## References

[1] Yu X, Cheng H, Zhang M, Zhao Y, Qu L and Shi G 2017 *Nat. Rev. Mater.* **2** 17046

[2] Sturala J, Luxa J, Pumera M and Sofer Z 2018 *Chem. Eur. J.* **24** 5992 – 6006

[3] Dasari B L, Nouri J M, Brabazon D and Naher S 2017 *Energy* **140** 766-778

[4] Karlicky F, Datta K K R, Otyepka M and Zboril R 2013 *ACS Nano* **7** 6434-6464

[5] Miao Q, Wang L, Liu Z, Wei B, Xu F and Fei W 2016 *Sci. Rep.* **6** 21832

[6] Zhang H et al. 2011 *Nano Lett.* **11** 4047-4051

[7] Zakeri M, Abouzari-Iotf E, Miayke M, Mehdipour-Ataei S and Shameli K 2019 *Arab. J. Chem.* **12** 188-197

[8] Rowley-Neale S J, Randviir E P, Dena A S A and Banks C E. 2018 *Appl. Mater. Today* **10** 218-226

[9] Guan L-Z, Zhao L, Wan Y-J and Tang L-C. 2018 *Nanoscale* **10** 14788-14811
[10] Fan M et al. 2016 *J. of Mat. Science* **51** 10323-10349
[11] Xu H, Ma L and Jin Z. 2018 *J. Energy Chem.* **27**, 146-160
[12] Wang Y, Shao Y, Matson DW, Li J and Lin Y 2010 *ACS Nano* **4** 1790–1798
[13] Deng D et al. 2011 *Chem. Mater.* **23** 1188
[14] Liu Y, et al. 2013 *Carbon* **60** 549–551
[15] Zhan C, Zhang Y, Cummings P T and Jiang D-E. 2016 *Phys. Chem. Chem. Phys.* **18** 4668–4674
[16] Wei D et al. 2015 *ACS Nano* **9** 164–171
[17] Soin N et al. 2011 *J. Phys. Chem. C* **115** 5366–5372
[18] Rybin M et al. 2016 *Carbon* **96** 196–202
[19] Liu J-Y, Chang H-Y, Quang Duc T and Ling Y-C. 2013 *J Mater. Chem. C* **1** 1713–1716
[20] Seo S., Yoon Y.H., Lee J.H., Park Y.H. and Lee, H. 2013 *ACS Nano* **7** 3607–3615
[21] Sliwak A, Grzyb B, Dıez N and Gryglewicz G. 2017 *Appl. Surf. Sci.* **399**, 265-271
[22] Schultz B J et al. 2014 *RSC Adv.* **4** 634-644
[23] Xue Y, Zhu L, Chen H, Qu J and Dai L 2015 *Carbon* **92** 305-310
[24] Nurunnabi M, Parvez K, Nafiujjaman M, Revuri V, Khan H A, Feng X and Lee Y-k 2015 *RSC Adv.* **5**, 42141-42161
[25] McCallion C, Burthem J, Rees-Unwin K, Golovanov A and Pluen A *Eur. J. Pharm. Biopharm.* 2016 **104** 235-250
[26] Brenner K and Murali R. 2011 *Appl. Phys. Lett.* **98** 113115
[27] Xu S et al. 2012 *Nano Res.* **5** 361–368
[28] Hummers W S and Offeman R E 1958 *J. Am. Chem. Soc.* **80** 1339
[29] Molodtsov S L et al. 2009 *Appl. Phys. A* **94** 501-505
[30] Kresse G, and Furthmüller 1996 *J. Phys. Rev. B* **54** 11169
[31] Blöchl P E. 1994 *Phys. Rev. B* **50** 17953
[32] Perdew J P, Burke K and Ernzerhof M 1996 *Phys. Rev. Lett.* **77** 3865
[33] Pavlov S V, Nazmutdinov R R, Fedorov M V and Kislenko S A. 2019 *J. Phys. Chem. C* **123** 6627-6634
[34] Elias D C et al. 2009 *Science* **323** 610-613
[35] Fan X B, Peng W, Li Y, Li X, Wang S, Zhang G and Zhang F 2008 *Adv. Mater*. **20** 4490–4493
[36] Rabchinskii M K et al. 2016 *J. Phys. Chem. C* **120** 28261-28269
[37] Li Y et al. 2012 *J. Mater. Chem*. **22** 15021−15024
[38] Perera S D, Mariano R G, Nijem N, Chabal Y, Ferraris J P and Balkus K J Jr 2012. *J. Power Sources* **215** 1−10
[39] Dreyer D R, Murali S, Zhu Y, Ruoff R S and Bielawski C W. 2011 *J. Mater. Chem.* **21** 3443–3447
[40] Rasul S, Alazmi A, Jaouen K, Hedhili M N and Costa P M F 2017 *Carbon* **111** 774-781
[41] Baldovino F H et al. 2016 *RSC Adv.* **6** 113924
[42] Du D, Li P and Ouyang J 2015 *ACS Appl. Mater. Interfaces* **7** 26952-26958
[43] Chua C K and Pumera M 2012 *J. Mater. Chem.* **22** 23227
[44] Shul'ga Y M, Vasilets V N, Baskakov S A, Muradyan V E, Skryleva E A and Parkhomenko Yu N 2012 *High Energ. Chem.* **46** 117–121
[45] Samanta K et al. 2013 *Chem. Commun.* **49** 8991-8993
[46] Beard B C. 1990 *Appl. Surf. Sci.* **45** 221-227
[47] Erden I, Keeffe J R, Xu F P and Zheng J B 1993 *J. Am. Chem. Soc.* **115** 9834-9835
[48] Kim S et al. 2012 *Nat. Mater.* **11** 544–549
[49] Chen J et al. 2016 *Chem. Sci.* **7** 1874-1881
[50] Yang S, Yue W, Huang D, Chen C, Lin H and Yang X. 2012 *RSC Advances* **2** 8827–8832
[51] Acik M, Lee G, Mattevi C, Chhowalla M, Cho K and Chabal Y J. 2010 *Nat. Mater.* **9** 840−845
[52] Ganguly A, Sharma S, Papakonstantinou P and Hamilton J 2011 *J. Phys. Chem. C* **115** 17009–17019
[53] Zheng W et al. 2018 *Chem. Commun.* **54** 13726-13729
[54] Bagri A, Mattevi C, Acik M, Chabal Y J, Chhowalla M and Shenoy V B 2010 *Nat. Chem.* **2** 581–587
[55] Larciprete R, Fabris S, Sun T, Lacovig P, Baraldi A and Lizzit S 2011 *J. Am. Chem. Soc.* **133** 17315–17321
[56] Gridnev A A, Gudkov M V, Bekhli L S and Mel'nikov V P 2018 *Rus. J. Phys. Chem. B* **12** 1008–1016
[57] Park S et al. 2012 *Nat. Commun.* **3** 638–645.
[58] Wei D, Liu Y, Wang Y, Zhang H, Huang L and Yu G 2009 *Nano Lett.* **9**, 1752–1758
[59] Mott N F, Pollitt M P S, Wallis S and Adkins C 1975 *J. Proc. R. Soc. Lond. A* **345** 169
[60] Khondaker S I, Shlimak I S, Nicholls J T, Pepper M and Ritchie D A 1991 *Phys. Rev. B* **59** 4580
[61] Efros A L and Shklovskii B I 1975 *J. Phys. C* **8** L49
[62] Shklovskii B I and Efros A 1984 *Electronic Properties of Doped Semiconductors* (Berlin: Springer-Verlag)
[63] Joung Da and Khondaker S I. 2012 *Phys. Rev. B* **86** 235423
[64] Ross M, Messai A M, Brice J, Saibal R and Somnath B 2012 *EPL (Europhysics Letters)* **97** 38001
[65] Eda G, Mattevi C, Yamaguchi H, Kim H, and Chhowalla M 2009 *J. Phys. Chem. C* **113** 15768
[66] Chang Y C and Haas S 2011 *Phys. Rev. B* **83** 085406
[67] Ugeda M M, Brihuega I, Guinea F and Gómez-Rodríguez J M 2010 *Phys. Rev. Lett.* **104** 096804
[68] Lu Y-F et al. 2013 *ACS Nano* **7** 6522–6532
[69] Chang D W, Choi H-J and Baek J-B 2015 *J. Mater. Chem. A* **3** 7659–7665
[70] Guo D, Shibuya R, Akiba C, Saji S, Kondo T and Nakamura J 2016 *Science* **351** 361–365
[71] Fujimoto Y and Saito S 2014 *J. Appl. Phys.* **115** 153701
[72] Van Lien N. 1995 *Phys. Lett. A* **207** 379-384
[73] Mkhoyan K A et al. 2009 *Nano Lett.* **9**, 1058
[74] Gómez-Navarro C et al 2010 *Nano Lett.* **10** 1144
[75] Zacharov I et al. 2019 *Open Engineering* **9** 512–520